SCIENTIFIC REPORTS

OPEN

SUBJECT AREAS:
NANOPARTICLES
COLLOIDS

Received
28 January 2014

Accepted
12 September 2014

Published
1 October 2014

Correspondence and requests for materials should be addressed to S.G. (sspsg2@iacs.res.in) or N.P. (camnp@iacs.res.in)

Tuning the Growth Pattern in 2D Confinement Regime of Sm_2O_3 and the Emerging Room Temperature Unusual Superparamagnetism

Amit K. Guria[1], Koushik Dey[2], Suresh Sarkar[1], Biplab K. Patra[1], Saurav Giri[2] & Narayan Pradhan[1]

[1]Department of Materials Science, Indian Association for the Cultivation of Science, Kolkata 700032, India, [2]Department of Solid State Physics, Indian Association for the Cultivation of Science, Kolkata 700032, India.

Programming the reaction chemistry for superseding the formation of Sm_2O_3 in a competitive process of formation and dissolution, the crystal growth patterns are varied and two different nanostructures of Sm_2O_3 in 2D confinement regime are designed. Among these, the regular and self-assembled square platelets nanostructures exhibit paramagnetic behavior analogous to the bulk Sm_2O_3. But, the other one, 2D flower like shaped nanostructure, formed by irregular crystal growth, shows superparamagnetism at room temperature which is unusual for bulk paramagnet. It has been noted that the variation in the crystal growth pattern is due to the difference in the binding ability of two organic ligands, oleylamine and oleic acid, used for the synthesis and the magnetic behavior of the nanostructures is related to the defects incorporated during the crystal growth. Herein, we inspect the formation chemistry and plausible origin of contrasting magnetism of these nanostructures of Sm_2O_3.

Nanomaterials exhibiting room temperature superparamganetism are under the limelight of nanoresearch for their unique applications in advanced technology including contrasting agent in Magnetic Resonance Imaging (MRI)[1–12] and targeted drug delivery[3–7,13]. Typically, superparamagnetism appears due to size effect in ferromagnetic or ferrimagnetic materials[2–4,9–11,14–18]. Magnetic anisotropy has the primary role for executing superparamagnetic behavior which decreases with volume of a material[19]. As a result, the magnetization can randomly flip under the influence of temperature and response to the applied magnetic field like a paramagnet. Normally, superparamagnetism appears below the Curie temperature. From technological point of view superparamagnetism is highly promising because of large moment and easy polarizability even toward weak magnetic field. The emergence of superparamagnetism at room temperature in a classical paramagnet is quite unusual because this has been commonly appeared due to size effect in ferromagnetic or ferrimagnetic substances. In this report we demonstrate a rare consequence of superparamagnetism in a 2D flower like shaped nanostructure of Sm_2O_3 which is a conventional paramagnet in bulk.

However, with the advances in the synthetic chemistry of nanomaterials, several size, shape and phase tunable materials in nano-regime exhibiting various new and even unusual materials properties are already developed[18,20–37]. Not only the size regime, but also the interface ligand chemistry, internal defects and doping of foreign impurity materials can induce such properties[16,23,25,33–36,38–52]. This has been enormously studied for nanoscale optical[22,24,34,35,37,38,42], electrical[34,37] as well as magnetic[18,25–36,38–52] materials. These are not only important for various practical utilities but also remained challenging for fundamental understanding. For example, emergence of ferromagnetism in ZnO and ZnS having Zn-d^{10} electronic configuration seems puzzling[26–28,38–43]. Similar unusual consequences in nanomagnetism and the fundamental aspects of such exotic results compatible with various applications remain elusive and need investigation in detail.

Programming the reaction parameters to promote the formation of the nanomaterials in a competitive process of formation and dissolution, we report here two distinct nanostructures in 2D confinement regime of Sm_2O_3 which usually act as classical paramagnet in bulk[53] and even in nanoregime[54]. Interestingly, among these two nanostructures, one having regular shape, square platelet, behaves paramagnetically as typical bulk paramagnet and the other having irregular shape, 2D flower like platelet, behaves unusually exhibiting superparamagnetism at

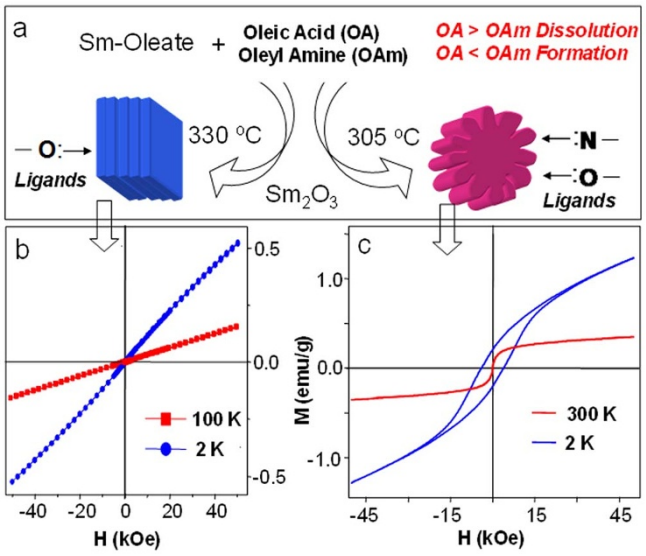

Figure 1 | Shape tuning of 2D nanostructures and their magnetization plots. (a) Schematic presentation of the synthetic procedure for the shape tuning in 2D confinement regime. (b) Magnetic hysteresis loops at 2 K and 100 K for plate like structure. (c) Magnetic hysteresis loops at 2 K and 300 K for flower like structure.

room temperature. A detailed analysis of these nanostructures has been carried out and their crystal growth patterns are correlated with their intricate magnetic behaviors.

Results

Shape tuning in 2D confinement and the different magnetic behaviors. For designing the nanostructures of Sm_2O_3, we explore here two most common organic capping ligands, oleylamine[55,56] and oleic acid[34,57]. Under certain ratio of these fatty amine and fatty acid, Sm-oleate is allowed to decompose at different reaction temperatures to obtain different shapes of Sm_2O_3 nanostructures. However, even both these organic ligands act as very good capping agents, here, fatty amine facilitates in formation of Sm_2O_3 by catalytic decomposition of Sm-oleate. In contrary, acid triggers the dissolution of the oxide to Sm-oleate. Hence, for the formation of the nanostructures, fatty amine to acid ratio and the reaction temperature are properly manipulated to an optimum condition for favoring the decomposition of the oleate precursor. In a typical reaction, with a particular ratio of fatty amine to acid, when the reaction is carried out at 330°C, square platelet shaped 2D nanostructures of Sm_2O_3 are obtained. In contrary, when the same reaction is carried out at 305°C, 2D flower shaped nanostructures are formed. Interestingly, these two shapes of Sm_2O_3 nanostructures show different magnetic behaviors. Though different kinds of nanostructures of Sm_2O_3 are already reported[54,58–62] including the square platelets and disks of other rare earth oxides[63–67], the intriguing 2D flower shaped nanostructures are new here. While several reported flower shaped nanomaterials[68,69] are in 3D but here we have observed the same in 2D and also via controlled growth. A schematic presentation of the synthetic processes of both nanostructures has been shown in Figure 1a and the difference in their magnetization behaviors is shown in Figure 1b and 1c. For the platelet shaped Sm_2O_3 structure, the plots exhibit straight line and pass through the origin which reflects its paramagnetic nature as observed in its bulk material. On the other hand, the 2D flower shaped structure shows nonlinear magnetization curves with a large coercivity at 2 K and superparamagnetic behavior at 300 K. To understand this distinct magnetic behavior, we study the shape evolution and crystal structures of these nanostructures in detail.

Crystal structure and crystal phase analysis. Figure 2a and 2b present TEM images of the square platelet shaped Sm_2O_3 obtained from different time intervals from a typical reaction at 330°C. Figure 2a shows the scattered platelets mostly lying horizontally on the TEM grid and Figure 2b presents the long range ordering of linearly packed platelets. The length of these square platelets is 50–60 nm. Figure 2c presents the magnified image of these self-assembled platelets and from this the width of these platelets are calculated ~1.2 nm.

Figure 2d–f presents the TEM images of the flower shaped structures in different resolutions obtained after 30 min of the reaction at 305°C (also see Supplementary Figure S1). Unlike square platelets, in

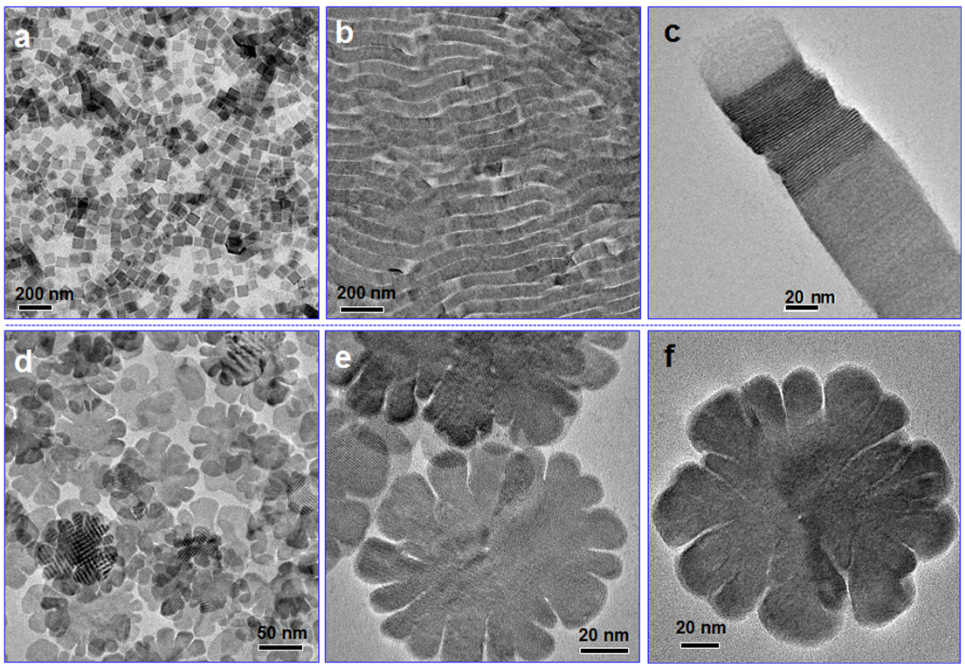

Figure 2 | Microscopic images of Sm_2O_3 nanostructures. (a) and (b) TEM images of the square nanoplatelets obtained at different time intervals of the reaction. (c) TEM image of stacked platelets in one column. (d–f) TEM images of the flower shaped 2D nanostructures of Sm_2O_3 in different resolutions.

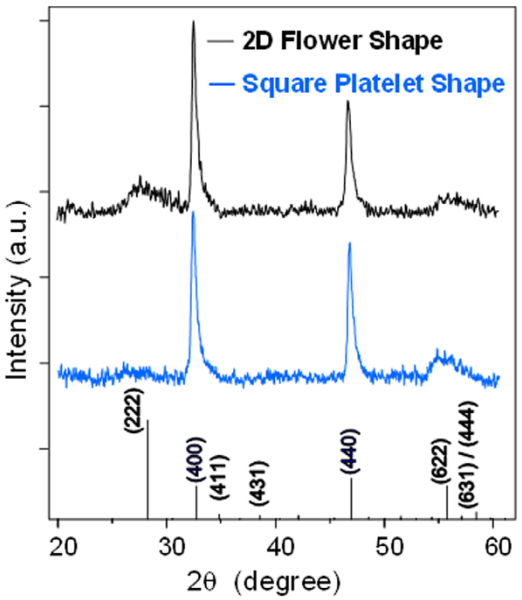

Figure 3 | XRD patterns for different shapes of Sm_2O_3 nanostructure. Black color XRD pattern represents for nanoflowers and the blue one for square platelets.

this case no self-assembly has been observed. These are also 2D platelets but the shapes are not regular like square platelets; rather possess several petals like arms. The 2D structure is further reflected from the moiré patterns appeared in the overlap zones shown in Figure 2d. Figure 2e and 2f present the images of single flower shaped structures and each of them having different number of arms. This suggests that the growth is not regular in this case. The length of these nanostructures remains 120–140 nm and width ~ 7 nm (Supplementary Figure S2).

Further to understand the phase of these structures, we have performed the powder XRD and analyzed the HRTEM images. It has been observed that both the nanostructures are in cubic phase. Figure 3 presents the XRD patterns for both these structures and the peaks resemble to the bulk cubic phase of Sm_2O_3 (ICSD # 165779). However, the small difference in the peak widths observed here might be due to the difference in the size, particularly the thickness difference of two different shaped nanostructures. Figure 4a and 4b show the HRTEM images of the flower shaped structures and the d-spacing of 0.545 and 0.38 nm correspond to {200} and (220) planes of cubic Sm_2O_3 respectively, and the image is viewed along [002] direction. An atomic model corresponds to this image has been shown in Figure 4c. Further, X-ray photoelectron spectra of these structures are analyzed and presence of only Sm^{3+} is confirmed (Supplementary Figure S3). From these results, it can be concluded here that the phase and oxidation states of the materials in these two shapes of nanostructures are same. Hence, the difference in the magnetic behavior might be originated from the difference in their crystal growth patterns. To understand more, we further study the origin of formation of these shapes of the nanostructures.

The interface ligand binding chemistry and the shape variation. From the synthetic protocols, it is revealed that in a particular ratio of amine to acid, the shapes the nanostructures are obtained due to variation of reaction temperature. Further, it is also observed that variation in the ratio of amine to acid also tunes the growth pattern and so also the shapes of the nanostructures. Interestingly, with excess acid or in only acid solution, no Sm_2O_3 is formed and the solution remains clear even for an hour (Table S1). On the other hand, with increase of fatty amine or in only amine solution, the decomposition proceeds faster and nanostructures are formed even at 250°C. To quantify the effect of amine to acid ratio with reaction temperature, we have studied here the decomposition process of the Sm-carboxylate precursor. From the thermogravimetric analysis, it has been observed that Sm-oleate decomposes at above 380°C (Supplementary Figure S4a) and interestingly, this decomposition temperature is lowered in presence of amine (Figure S4b). This suggests that amine catalyzes the thermal decomposition of Sm-oleate and more the amine content faster is the decomposition of the precursor. Hence, it can be concluded here that fatty amine to acid ratio in the reaction mixture controls the decomposition of the precursor and governs the morphology of the nanostructures at different reaction temperatures.

However, to further understand the difference in the shape evolution, we have carried out the elemental analysis for both flower and square platelet shapes, and it is observed that the square platelets shaped structures contains insignificant amount of N (from C H N analysis). This indicates that acids are mostly act here as capping agent. In contrary, flower shaped structures have both amine and acid. From this observation it is evident that both acid and amine act as ligand at 305°C, but acid is more active ligand at 330°C. It is also known that amine is more volatile than acid at 330°C. Moreover, 330°C is close to the boiling point of oleylamine (345°C). Hence, oleylamine is more labile at 330°C and it only helps in decomposing the Sm-oleate but cannot actively participate as capping agent. As a result, the oxide formed at this temperature is predominantly capped with oleic acid and the growth remains regular leading to square platelet shape of the nanostructures But, on reduction of the temperature to 305°C, the mobility of the amines reduces to some extent and hence both acid and amine act as the surface ligands. However, amines are being more labile and weak binding ligands, the cationic sites bonded with amine (-N) would be more facilitated for faster growth in comparison to acid bonded sites. Hence, irregular growth is expected at this temperature. The intermediate sample shows that these flowers are in fact formed via circular disks (Supplementary

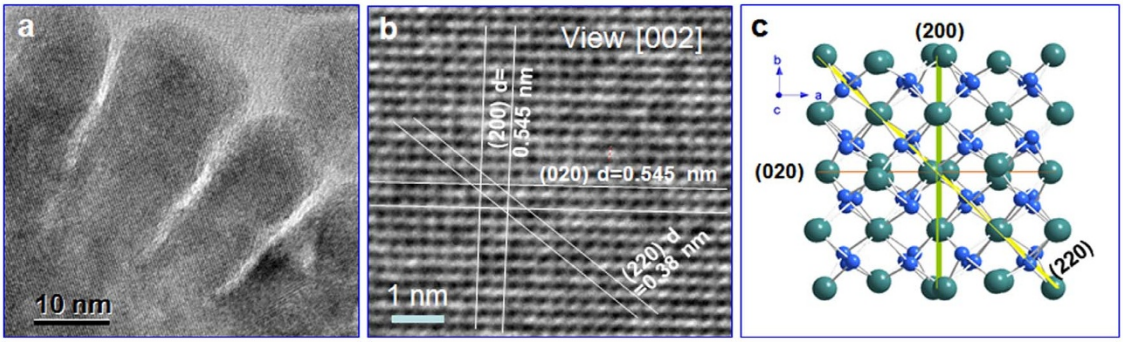

Figure 4 | HRTEM analysis. (a) and (b) HRTEM images of a part of the flower shaped nanostructures. (c) The atomic model of cubic phased Sm_2O_3.

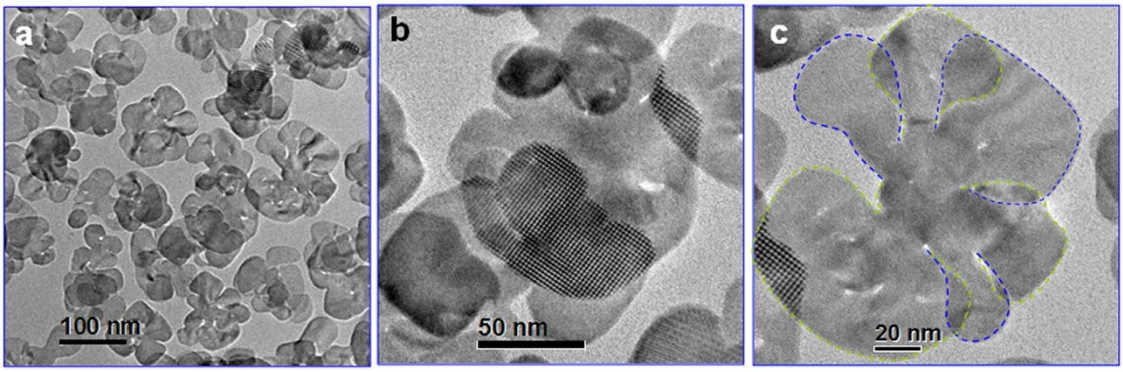

Figure 5 | Intermediate TEM image showing the growth pattern. (a–c) TEM images of different resolutions of the sample collected during the formation of nanoflower. (b) Shows the moire pattern which indicates the 2D shape and (c) presents the flower shape with outline marks for the growth pattern of the petals.

Figure S2). Figure 5 shows the TEM images of sample collected after the disk formation but before the flower formation and these clearly indicate the random growth occurs from particular peripheral part of circular disk. But, to confirm whether the fatty acid hinders the regular growth we have tried to carry out several reactions with decreasing the acid and increasing the amine content in the reaction mixture. Interestingly, 2D circular disks are formed when amine concentration is increased (amine : acid = 6 : 1) (Supplementary Figure S5a). This concludes that while excess amine remains in the solution, the structure does not turn to flower shape. Here, prompt availability of the ligands slow down the growth process and allows the nanocrystals to grow more smoothly as well as slowly. Interestingly, when the reaction temperature is further reduced with this increased amine content, also similar 2D circular disks are formed and this further supports that low temperature reduces the lability of the amine ligands on the nanocrystals surface and hence hinders the flower shape formation. Hence, we can conclude that in a balanced ratio of amine to acid, the interface binding chemistry controls the growth and this in turn determines the shape of the nanostructures.

Para- and the induced superparamagnetism. As stated in Figure 1, the two shapes of nanostructures have different magnetic behaviors. To understand this and further to correlate the chemistry of formation of the shapes, we first investigated in details of the magnetization for both cases. Thermal variation of zero-field cooled and field-cooled magnetization recorded at 100 Oe are depicted in Figure 6a and 6b for square platelet and flower shaped nanostructures, respectively. Although measurements are carried out at a fixed magnetic field, the value of magnetization is $\sim 10^2$ times higher for the flower shaped nanostructures. In compatible with the bulk counterpart typical paramagnetic-like temperature dependence of magnetization is observed where zero-field and field-cooled magnetization overlap each other over the measure temperature range for square platelet shaped nanostructures. In contrast, a well defined peak in zero-field cooled magnetization is

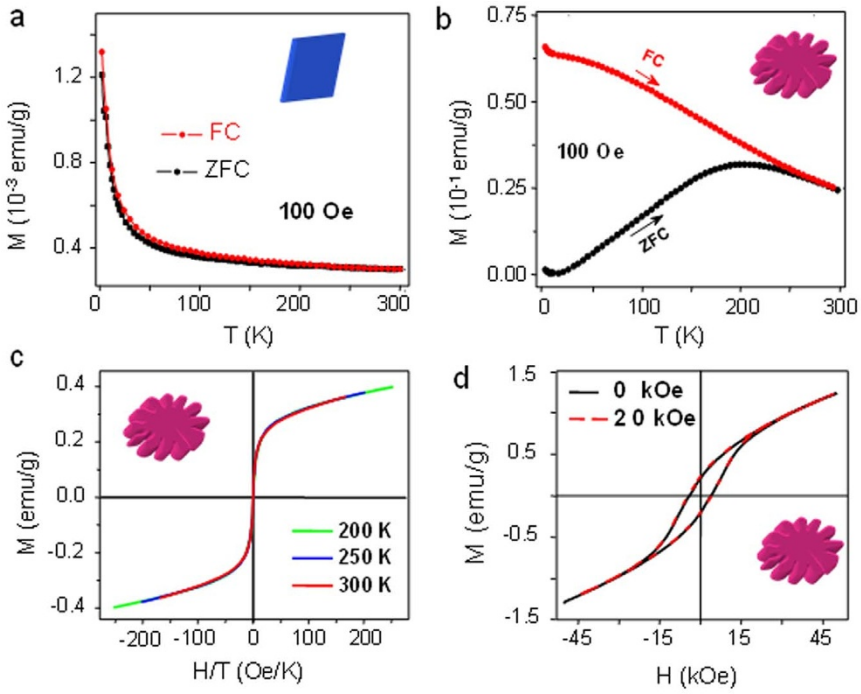

Figure 6 | Para- and superparamagnetism. Temperature dependence of ZFC and FC magnetization measured at a field (H) = 100 Oe for (a) plate like structure and (b) flower like structure. (c) The plots of magnetization against H/T at 200 K, 250 K and 300 K. (d) MH loops at 2 K at H_{cool} = 0 and 20 kOe.

evident for the flower shaped nanostructures. Field-cooled magnetization continues to increase with decreasing temperature as typically expected below the noninteracting or weakly interacting superparamagnetic blocking process[70]. As shown in Figure 1c, magnetization curve at 2 K has got large magnetic coercivity which almost vanishes at 150 K (Supplementary Figure S6). The superparamagnetic regime is distinguished by plotting the scaled magnetization curves and is further supported by the absence of coercivity for $T > T_B$ (blocking temperature)[71]. Figure 6c displays plots of scaled magnetization curves at $T > T_B$ which clearly follow a master curve emphasizing superparamagnetic behavior. Enlarged view of the magnetization curves above T_B does not show convincing coercivity further designating a superparamagnetic response. Thermal variation of zero-field cooled magnetization recorded at different field (Supplementary Figure S7) demonstrates that T_B decreases with increasing applied magnetic field following Almeida-Thouless (AT) line (Supplementary Figure S8). This AT line has been reported for superparamagnetic blocking temperature.

Magnetic hysteresis loops at 2 K are shown in Figure 6d which are measured after zero-field cooling and field-cooling (20 kOe) protocols. A significant coercivity of 3.93 kOe is observed at 2 K for zero-field cooled curve. Magnetization curve at 2 K does not show saturating trend even at 50 kOe (Supplementary Figure S9). In case of crystal field splitting spins are doubly populated and fifth unpaired spin provides effectively $J = 1/2$ for $^6H_{5/2}$ of Sm^{3+}. Thus, $J = 1/2$ provides 1.0 μ_B which is still much larger than observed value of magnetization at 2 K ($\sim$0.08 μ_B at 50 kOe). This indicates that magnetization at 2 K is much below the expected saturated value. Interestingly, a considerable shift (Supplementary Figure S10 for more clarity in enlarged scale) in the magnetic hysteresis loop is observed when material is cooled in 20 kOe from a temperature above T_B. The shift in the magnetic hysteresis loop is a typical manifestation of exchange bias effect[72] which is attractive for the technological applications[73]. Exchange bias is an intricate phenomenon which is occurred at the interface between two magnetic phases having significant difference in magnetic anisotropy. This was first discovered in a Co/CoO nanoparticle where antiferromagnetic CoO component pins the ferromagnetic Co spins at the interface between them due to field cooling process[74]. Even after the discovery of exchange bias for more than five decades, origin of the phenomenon remains elusive because of interface mechanism and it occurs in various combination of magnetic phases. Here, the magnitude of exchange bias field is significant as $\sim$260 Oe, which decreases sharply with increasing temperature (Supplementary Figure S11) and nearly vanishes close to 50 K. Emergence of exchange bias effect for 2D flower shaped Sm_2O_3 is special, because Sm_2O_3 is a classical paramagnet in bulk state and even in nanostructures with different particle shapes[54]. Evidence of exchange bias effect involving a paramagnetic substance is interesting which has been rarely reported so far[75]. We carefully note that appearance of exchange bias field is associated with the low temperature increase of magnetization in zero-field cooled magnetization as evident for the high field measurements (Supplementary Figure S7). The low temperature increase of magnetization indicates emergence of an uncompensated ferromagnetic component. Since appearance of exchange bias effect confirms magnetic phase coexistence, we propose a magnetic phase separation between ferromagnetic shell and paramagnetic-like core in the 2D flower shaped nanostructure of Sm_2O_3 and pinning mechanism at the interface between these two gives rise to the exchange bias effect due to field cooling process. The ferromagnetic component appeared as a fraction of nanostructured flower apparently causes superparamagnetic response above the blocking temperature. As it has been recognized that superparamagnetic state appears below the Curie temperature of nanostructured ferromagnetic or ferrimagnetic particles, the ferromagnetic component conjectured from the low temperature increase of magnetization and appearance of exchange bias effect in the current investigation leads to the observed blocking process and superparamagnetic response due to size effect in nanoscale.

Discussion

The appearance of this superparamagnetism at room temperature from the induced ferromagnetism of the bulk paramagnetic material is unique and to our knowledge this has not been observed earlier. To understand the origin of this unusual behavior we correlate the chemistry of formation, the interface chemistry and defects incorporated during growth of the nanostructures. It is reported that the amine and acid sintered material can lead to different magnetism[44] and as in our case the activities of these ligands play crucial role in shape evolution, the magnetism might be obtained from the surface defects due to difference in the binding ability of –N and –O. For pure acid ligands less oxygen vacancy is expected as it is coordinated to metal ions via oxygen. On the other hand for amine and acid cases, amine may create more surface oxygen vacancy. Also, as amines are labile, more number of unsaturated surface bonds is expected. These might create the unusual magnetism. On contrary the nanostructures obtained with excess amine (Supplementary Figure S5a) show paramagnetic behavior (Supplementary Figure S5b). Hence, the induced ferromagnetism and resulting superparamagnetism cannot be due to the surface ligands. The other possibility is the internal defects of the nanostructures due to the peculiar growth pattern of the flower shaped nanostructure. Literature survey reveals that internal defect like oxygen vacancy induces ferromagnetism in oxide materials[49,51]. Close observation of the XPS spectra of O1s suggests that their intensity and positions differ to some extent in these two structures. However, we could not quantify the O-defects as many oxygen species contribute to this data (see Supplementary Figure S3c and subsequent discussion). But, from our experimental results the origin of the differences in magnetism is clearly manifested from the difference in the growth pattern. To understand this, we compare the magnetism of the circular plates nanostructures obtained at lower reaction temperature (280°C) or trapped before the nanoflowers formation at 305°C with the flower and square shaped nanostructures. For quantitative observation, we have carried out the synthesis of all these nanostructures in a single lot reaction where three parts have been annealed at 280°C, 305°C as well as 330°C. From the obtained nanostructure, only the flower shaped structure showed the unusual magnetic behavior and all other reflected the paramagnetism. This clearly states that the growth pattern in the flower shaped structures is responsible for this change in magnetic behavior and also rules out the effects of any impurity additionally present in the reaction system or the surface ligands. This is also supported with elemental mapping which suggests the materials contain only Sm and O (Supplementary Figure S12).

Further, as the particular flower shape shows this unusual magnetism, we have tried to detect the possible reaction stage of induction of defects in the nanostructures. The usual paramagnetism obtained from the early stage sample clearly suggests that the peculiarity comes from the fast arm growth typically observed due to competitive ligands binding at the interface. The observed exchange bias effect also supports the coexistence of two magnetic phases. So we can assume that paramagnetic disk is surrounded with ferromagnetic arms. Hence, we can propose here that the fast growth for the formation of petal like arms on the shell of circular disks leads to irregular packing of Sm and O atoms and this creates defects which in turn induce the superparamagnetism at room temperature as stated earlier.

In conclusion, we report here the interface chemistry for driving two different types of 2D crystal growth patterns leading to two distinct shapes of Sm_2O_3 nanostructures in same confinement regime and identical crystal phase. However, interestingly these two shapes show different magnetic behaviors: one resembles with

the bulk paramagnet and other act as unusual superparamagnet at room temperature. The results suggest that implementation of novel chemistry can alter the crystal growth and induce new physical properties, important for both fundamental understanding and practical applications.

Methods

Chemicals. Samarium(III) acetate hydrate [$Sm(OAc)_3.xH_2O$, 99.9%], oleic acid (OA, tech, 90%), oleylamine (OAm, tech, 70%) were purchased from Sigma-Aldrich. All chemicals were used without any further purification.

Synthesis of flower shaped Sm_2O_3. In a typical synthesis, 0.2 mmol $Sm(OAc)_3.xH_2O$ (65.50 mg) and 2 mL OA (6.28 mmol) were taken in a 25 mL three-neck flask equipped with a condenser, thermocouple, septum, and containing a magnetic stir bar. The reaction flask was sealed and placed in a heating mantle on a stir plate. After the flask was degassed with N_2 bubbling for 10 minutes at 80°C, it was heated to 260°C. 2 mL OAm (6.08 mmol) was then swiftly injected into the flask through the septum using a syringe and the mixture was kept at 260°C for 45 minutes with stirring to remove any residual water. Then the temperature was set at 305°C. The mixture was vigorously stirred at this temperature for 20 min after the appearance of white turbidity to the yellow solution. Finally, the reaction mixture was cooled down to room temperature and the nanocrystals were purified using hot ethanol as non solvents and chloroform as dispersing solvent.

Synthesis of square nanoplates of Sm_2O_3. Square nanoplates of Sm_2O_3 were obtained following the procedure as stated above for flower shape except by annealing the mixture solution at 330°C instead of 305°C.

The same nanostructures were obtained when a degassed solution of $Sm(OAc)_3.xH_2O$ in OAm was injected at 260°C to degassed OA in flask following the similar procedure as stated above.

Materials characterization. Transmission Electron Microscopy (TEM), High Resolution Transmission Electron Microscopy (HRTEM) and Scanning Transmission Electron Microscopy (STEM) images were taken on a UHR-FEG-TEM, JEOL, JEM 2100 F model using 200 kV electron source. Specimens were prepared by dropping a drop of purified nanocrystals solution in chloroform on a carbon coated copper grid, and the grid was dried in air. X-ray Powder Diffraction (XRD) of the purified sample was taken at room temperature by Bruker D8 Advance powder diffractometer, using Cu Kα ($\lambda = 1.5406$ Å) as the incident radiation. X-ray Photoelectron Spectroscopy (XPS) measurements were performed at room temperature using Al Kα source (10 mA, 15 kV) on a laboratory based commercial X-ray photoelectron spectrometer from Omicron Nanotechnology. Thermogravimetric Analysis (TGA) was performed with a thermal analyzer TA-SDT Q-600 system equipped with an alumina pan at heating rate 10°C/min under N_2 environment. Magnetic measurements were performed using a commercial superconducting quantum interference device (SQUID) magnetometer of Quantum Design (MPMS XL, Evercool model).

1. Na, H. B., Song, I. C. & Hyeon, T. Inorganic Nanoparticles for MRI Contrast Agents. *Adv. Mater.* **21**, 2133–2148 (2009).
2. Zhao, Z. *et al.* Octapod iron oxide nanoparticles as high-performance T_2 contrast agents for magnetic resonance imaging. *Nat. commun.* **4**, 2266 (2013).
3. Laurent, S. *et al.* Magnetic Iron Oxide Nanoparticles: Synthesis, Stabilization, Vectorization, Physicochemical Characterizations, and Biological Applications. *Chem. Rev.* **108**, 2064–2110 (2008).
4. Tassa, C., Shaw, S. Y. & Weissleder, R. Dextran-Coated Iron Oxide Nanoparticles: A Versatile Platform for Targeted Molecular Imaging, Molecular Diagnostics, and Therapy. *Acc. Chem. Res.* **44**, 842–852 (2011).
5. Gao, J., Gu, H. & Xu, B. Multifunctional Magnetic Nanoparticles: Design, Synthesis, and Biomedical Applications. *Acc. Chem. Res.* **42**, 1097–1107 (2009).
6. McCarthy, J. R. & Weissleder, R. Multifunctional magnetic nanoparticles for targeted imaging and therapy. *Adv. Drug Deliv. Rev.* **60**, 1241–1251 (2008).
7. Mornet, S. *et al.* Magnetic nanoparticle design for medical applications. *Prog. in Solid State Chem.* **34**, 237–247 (2006).
8. Corot, C., Robert, P., Idee, J.-M. & Port, M. Recent advances in iron oxide nanocrystal technology for medical imaging. *Adv. Drug Deliv. Rev.* **58**, 1471–1504 (2006).
9. Weissleder, R. *et al.* Ultrasmall superparamagnetic iron oxide: characterization of a new class of contrast agents for MR imaging. *Radiology* **175**, 489–493 (1990).
10. Kim, B. H. *et al.* Large-Scale Synthesis of Uniform and Extremely Small-Sized Iron Oxide Nanoparticles for High-Resolution T1 Magnetic Resonance Imaging Contrast Agents. *J. Am. Chem. Soc.* **133**, 12624–12631 (2011).
11. Lee, N. & Hyeon, T. Designed synthesis of uniformly sized iron oxide nanoparticles for efficient magnetic resonance imaging contrast agents. *Chem. Soc. Rev.* **41**, 2575–2589 (2012).
12. Di Marco, M. *et al.* Physicochemical characterization of ultrasmall superparamagnetic iron oxide particles (USPIO) for biomedical application as MRI contrast agents. *Int. J. Nanomededicine* **2**, 609–622 (2007).
13. Wahajuddin & Arora, S. Superparamagnetic iron oxide nanoparticles: magnetic nanoplatforms as drug carriers. *Int. J. Nanomededicine* **7**, 3445–3471 (2012).
14. Li, X.-H. *et al.* Synthesis and magnetic properties of nearly monodisperse $CoFe_2O_4$ nanoparticles through a simple hydrothermal condition. *Nano. Res. Lett.* **5**, 1039–1044 (2010).
15. Skumryev, V. *et al.* Beating the superparamagnetic limit with exchange bias. *Nature* **423**, 850–853 (2003).
16. Mikhaylova, M. *et al.* Superparamagnetism of Magnetite Nanoparticles: Dependence on Surface Modification. *Langmuir* **20**, 2472–2477 (2004).
17. Bao, N. *et al.* Controlled Growth of Monodisperse Self-Supported Superparamagnetic Nanostructures of Spherical and Rod-Like $CoFe_2O_4$ Nanocrystals. *J. Am. Chem. Soc.* **131**, 12900–12901 (2009).
18. Zheng, W. *et al.* Quantum Phase Transition from Superparamagnetic to Quantum Superparamagnetic State in Ultrasmall $Cd_{1-x}Cr(II)_xSe$ Quantum Dots? *J. Am. Chem. Soc.* **134**, 2172–2179 (2012).
19. Jamet, M. *et al.* Magnetic Anisotropy of a Single Cobalt Nanocluster. *Phys. Rev. Lett.* **86**, 4676–4679 (2001).
20. Park, J., Joo, J., Kwon, S. G., Jang, Y. & Hyeon, T. Synthesis of monodisperse spherical nanocrystals. *Angew. Chem., Int. Ed.* **46**, 4630–4660 (2007).
21. El-Sayed, M. A. Small is different: Shape-, size-, and composition-dependent properties of some colloidal semiconductor nanocrystals. *Acc. Chem. Res.* **37**, 326–333 (2004).
22. Murray, C. B., Norris, D. J. & Bawendi, M. G. Synthesis and characterization of nearly monodisperse CdE (E = sulfur, selenium, tellurium) semiconductor nanocrystallites. *J. Am. Chem. Soc.* **115**, 8706–8715 (1993).
23. Yin, Y. & Alivisatos, A. P. Colloidal nanocrystal synthesis and the organic-inorganic interface. *Nature* **437**, 664–670 (2005).
24. Peng, X. Band Gap and Composition Engineering on a Nanocrystal in Solution. *Acc. Chem. Res.* **43**, 1387–1395 (2010).
25. Magana, D., Perera, S. C., Harter, A. G., Dalal, N. S. & Strouse, G. F. Switching-on Superparamagnetism in Mn/CdSe Quantum Dots. *J. Am. Chem. Soc.* **128**, 2931–2939 (2006).
26. Zhu, G., Zhang, S., Xu, Z., Ma, J. & Shen, X. Ultrathin ZnS Single Crystal Nanowires: Controlled Synthesis and Room-Temperature Ferromagnetism Properties. *J. Am. Chem. Soc.* **133**, 15605–15612 (2011).
27. Liu, C., Yun, F. & Morko, H. Ferromagnetism of ZnO and GaN: a review. *J. Mater. Sci.: Mater. Electron.* **16**, 555–597 (2005).
28. Kapilashrami, M., Xu, J., Stroem, V., Rao, K. V. & Belova, L. Transition from ferromagnetism to diamagnetism in undoped ZnO thin films. *Appl. Phys. Lett.* **95**, 033104 (2009).
29. Hou, Y. *et al.* A facile synthesis of $SmCo_5$ magnets from core/shell Co/Sm_2O_3 nanoparticles. *Adv. Mater.* **19**, 3349–3352 (2007).
30. Zheng, L. *et al.* Core/shell $SmCo_5/Sm_2O_3$ magnetic composite nanoparticles. *J. Nanopart. Res.* **14**, 1129 (2012).
31. Sundaresan, A., Bhargavi, R., Rangarajan, N., Siddesh, U. & Rao, C. N. R. Ferromagnetism as a universal feature of nanoparticles of the otherwise nonmagnetic oxides. *Phys. Rev. B* **74**, 161306 (2006).
32. Granitzer, P. *et al.* Investigation of a mesoporous silicon based ferromagnetic nanocomposite. *Nano. Res. Lett.* **5**, 374–378 (2010).
33. Kim, H.-J. *et al.* Nature of magnetic impurity induced superparamagnetism and anomalous Hall effect in β-$FeSi_2$ single crystals. *Physica B* **407**, 126–130 (2012).
34. Ghosh, S., Das, K., Chakrabarti, K. & De, S. K. Effect of oleic acid ligand on photophysical, photoconductive and magnetic properties of monodisperse SnO2 quantum dots. *Dalton Trans.* **42**, 3434–3446 (2013).
35. Li, J.-M., Zeng, X.-L., Dong, Y.-H. & Xu, Z.-A. White-light emission and weak antiferromagnetism from cubic rare-earth oxide Eu_2O_3 electrospun nanostructures. *CrystEngComm* **15**, 2372–2377 (2013).
36. Wang, D. *et al.* Robust Room-Temperature Ferromagnetism with Giant Anisotropy in Nd-Doped ZnO Nanowire Arrays. *Nano Lett.* **12**, 3994–4000 (2012).
37. Jana, S., Srivastava, B. B., Jana, S., Bose, R. & Pradhan, N. Multifunctional Doped Semiconductor Nanocrystals. *J. Phys. Chem. Lett.* **3**, 2535–2540 (2012).
38. Xing, G. *et al.* Correlated d^0 ferromagnetism and photoluminescence in undoped ZnO nanowires. *Appl. Phys. Lett.* **96**, 112511 (2010).
39. Liu, W., Li, W., Hu, Z., Tang, Z. & Tang, X. Effect of oxygen defects on ferromagnetic of undoped ZnO. *J. Appl. Phys.* **110**, 013901 (2011).
40. Peng, C. *et al.* Possible Origin of Ferromagnetism in an Undoped ZnO d^0 Semiconductor. *J. Phys. Chem. C* **116**, 9709–9715 (2012).
41. Xu, X. *et al.* Size Dependence of Defect-Induced Room Temperature Ferromagnetism in Undoped ZnO Nanoparticles. *J. Phys. Chem. C* **116**, 8813–8818 (2012).
42. Panigrahy, B., Aslam, M., Misra, D. S., Ghosh, M. & Bahadur, D. Defect-Related Emissions and Magnetization Properties of ZnO Nanorods. *Adv. Funct. Mater.* **20**, 1161–1165 (2010).
43. Garcia, M. A. *et al.* Magnetic Properties of ZnO Nanoparticles. *Nano Lett.* **7**, 1489–1494 (2007).
44. Kittilstved, K. R. & Gamelin, D. R. Activation of High-TC Ferromagnetism in Mn^{2+}-Doped ZnO using Amines. *J. Am. Chem. Soc.* **127**, 5292–5293 (2005).
45. Sundaresan, A. & Rao, C. N. R. Ferromagnetism as a universal feature of inorganic nanoparticles. *Nano Today* **4**, 96–106 (2009).

46. MacManus-Driscoll, J. L., Khare, N., Liu, Y. & Vickers, M. E. Structural evidence for Zn interstitials in ferromagnetic $Zn_{1-x}Co_xO$ films. *Adv. Mater.* **19**, 2925–2929 (2007).
47. Zheng, W. & Strouse, G. F. Involvement of Carriers in the Size-Dependent Magnetic Exchange for Mn:CdSe Quantum Dots. *J. Am. Chem. Soc.* **133**, 7482–7489 (2011).
48. Archer, P. I., Radovanovic, P. V., Heald, S. M. & Gamelin, D. R. Low-Temperature Activation and Deactivation of High-Curie-Temperature Ferromagnetism in a New Diluted Magnetic Semiconductor: Ni^{2+}-Doped SnO_2. *J. Am. Chem. Soc.* **127**, 14479–14487 (2005).
49. Parras, M. *et al.* Room-Temperature Ferromagnetism in Reduced Rutile $TiO_{2-\delta}$ Nanoparticles. *J. Phys. Chem. Lett.* **4**, 2171–2176 (2013).
50. Kittilstved, K. R., Liu, W. K. & Gamelin, D. R. Electronic structure origins of polarity-dependent high-T_C ferromagnetism in oxide-diluted magnetic semiconductors. *Nat. Mater.* **5**, 291–297 (2006).
51. Chen, S.-Y., Lu, Y.-H., Huang, T.-W., Yan, D.-C. & Dong, C.-L. Oxygen Vacancy Dependent Magnetism of CeO_2 Nanoparticles Prepared by Thermal Decomposition Method. *J. Phys. Chem. C* **114**, 19576–19581 (2010).
52. Zhang, L. *et al.* Regulation of Magnetic Behavior and Electronic Configuration in Mn-Doped ZnO Nanorods through Surface Modifications. *Chem. Mater.* **24**, 1676–1681 (2012).
53. Kittel, C. *Introduction to Solid State Physics* (John Wiley & Sons Inc, New York, 1976).
54. Ghosh, P. *et al.* Synthesis and characterization of different shaped Sm_2O_3 nanocrystals. *J. Phys. D: Appl. Phys.* **43**, 405401 (2010).
55. Mourdikoudis, S. & Liz-Marzan, L. M. Oleylamine in Nanoparticle Synthesis. *Chem. Mater.* **25**, 1465–1476 (2013).
56. Xu, Z., Shen, C., Hou, Y., Gao, H. & Sun, S. Oleylamine as both reducing agent and stabilizer in a facile synthesis of magnetite nanoparticles. *Chem. Mater.* **21**, 1778–1780 (2009).
57. Hou, Y., Xu, Z. & Sun, S. Controlled synthesis and chemical conversions of FeO nanoparticles. *Angew. Chem., Int. Ed.* **46**, 6329–6332 (2007).
58. Nguyen, T.-D., Mrabet, D. & Do, T.-O. Controlled Self-Assembly of Sm_2O_3 Nanoparticles into Nanorods: Simple and Large Scale Synthesis using Bulk Sm_2O_3 Powders. *J. Phys. Chem. C* **112**, 15226–15235 (2008).
59. Dakhel, A. A. Dielectric and optical properties of samarium oxide thin films. *J. Alloys Compd.* **365**, 233–239 (2004).
60. Liu, T., Zhang, Y., Shao, H. & Li, X. Synthesis and Characteristics of Sm_2O_3 and Nd_2O_3 Nanoparticles. *Langmuir* **19**, 7569–7572 (2003).
61. Liu, P., Wang, Y., Wang, X., Yang, C. & Yi, Y. Polypyrrole-coated samarium oxide nanobelts: fabrication, characterization, and application in supercapacitors. *J. Nanopart. Res.* **14**, 1232 (2012).
62. Huang, S.-Y. *et al.* Resistive switching characteristics of Sm_2O_3 thin films for nonvolatile memory applications. *Solid-State Electron.* **63**, 189–191 (2011).
63. Si, R., Zhang, Y.-W., You, L.-P. & Yan, C.-H. Rare-earth oxide nanopolyhedra, nanoplates, and nanodisks. *Angew. Chem., Int. Ed.* **44**, 3256–3260 (2005).
64. Cao, Y. C. Synthesis of Square Gadolinium-Oxide Nanoplates. *J. Am. Chem. Soc.* **126**, 7456–7457 (2004).
65. Bailey, M. J., van der Weegen, R., Klemm, P. J., Baker, S. L. & Helms, B. A. Stealth Rare Earth Oxide Nanodiscs for Magnetic Resonance Imaging. *Adv. Healthcare Mater.* **1**, 437–442 (2012).
66. Si, R., Zhang, Y.-W., Zhou, H.-P., Sun, L.-D. & Yan, C.-H. Controlled-Synthesis, Self-Assembly Behavior, and Surface-Dependent Optical Properties of High-Quality Rare-Earth Oxide Nanocrystals. *Chem. Mater.* **19**, 18–27 (2006).
67. Huo, Z. *et al.* Self-Organized Ultrathin Oxide Nanocrystals. *Nano Lett.* **9**, 1260–1264 (2009).
68. Narayanaswamy, A., Xu, H., Pradhan, N. & Peng, X. Crystalline Nanoflowers with Different Chemical Compositions and Physical Properties Grown by Limited Ligand Protection. *Angew. Chem., Int. Ed.* **45**, 5361–5364 (2006).
69. Wang, Y. *et al.* A facile approach to PbS nanoflowers and their shape-tunable single crystal hollow nanostructures: Morphology evolution. *CrystEngComm* **13**, 199–203 (2011).
70. Luo, W., Nagel, S. R., Rosenbaum, T. F. & Rosensweig, R. E. Dipole interactions with random anisotropy in a frozen ferrofluid. *Phys. Rev. Lett.* **67**, 2721–2724 (1991).
71. Bedanta, S. & Kleemann, W. Supermagnetism. *J. Phys. D: Appl. Phys.* **42**, 013001 (2009).
72. Giri, S., Patra, M. & Majumdar, S. Exchange bias effect in alloys and compounds. *J. Phys.: Condens. Matter* **23**, 073201 (2011).
73. Nogues, J. & Schuller, I. K. Exchange bias. *J. Magn. Magn. Mater.* **192**, 203–232 (1999).
74. Meiklejohn, W. H. & Bean, C. P. New magnetic anisotropy. *Phys. Rev.* **102**, 1413 (1956).
75. Cai, J. W., Liu, K. & Chien, C. L. Exchange coupling in the paramagnetic state. *Phys. Rev. B* **60**, 72–75 (1999).

Acknowledgments

DST and CSIR of India are acknowledged for funding. N.P. and A.K.G. acknowledge DST Swarnajayanti and CSIR SPMF for fellowship.

Author contributions

A.K.G. performed the most part of the synthetic experiments; K.D. and S.G. performed the magnetic measurements and analyzed the data; S.S., B.K.P. and N.P. helped with problem designing, results analysis, and wrote the paper.

Additional information

Supplementary information accompanies this paper at http://www.nature.com/scientificreports

Competing financial interests: The authors declare no competing financial interests.

How to cite this article: Guria, A.K. *et al.* Tuning the Growth Pattern in 2D Confinement Regime of Sm_2O_3 and the Emerging Room Temperature Unusual Superparamagnetism. *Sci. Rep.* **4**, 6514; DOI:10.1038/srep06514 (2014).